

Influence of the iron spin crossover in ferropericlase on the lower mantle geotherm

Juan J. Valencia-Cardona,¹ Gaurav Shukla,² Zhongqing Wu³, Christine

Houser⁴, David A. Yuen^{1,5}, Renata M. Wentzcovitch,^{1,2}

arXiv:1610.08412v2 [physics.geo-ph] 28 Oct 2016

Corresponding author: Juan J. Valencia-Cardona, Scientific Computing Program, University of Minnesota, Minneapolis, Minnesota, USA. (valen167@umn.edu)

¹Scientific Computing Program,
University of Minnesota, Minneapolis,
Minnesota, USA

²Department of Chemical Engineering
and Materials Science, University of
Minnesota, Minneapolis, Minnesota, USA

³School of Earth and Space Sciences,
University of Science and Technology of
China, Hefei, Anhui, China

⁴Earth-Life Science Institute, Tokyo
Institute of Technology, Tokyo, Japan

⁵Department of Earth Sciences,
University of Minnesota, Minneapolis, USA

The iron spin crossover in ferropericlase introduces anomalies in its thermodynamics and thermoelastic properties. Here we investigate how these anomalies can affect the lower mantle geotherm. The effect is examined in mantle aggregates consisting of mixtures of bridgmanite, ferropericlase, and CaSiO_3 perovskite, with different Mg/Si ratios varying from harzburgitic to perovskitic (Mg/Si \sim 1.5 to 0.8). We find that the anomalies introduced by the spin crossover increase the isentropic gradient and thus the geotherm proportionally to the amount of ferropericlase. The geotherms can be as much as $\sim 200\text{K}$ hotter than the conventional adiabatic geotherm at deep lower mantle conditions. Aggregate elastic moduli and seismic velocities are also sensitive to the spin crossover and the geotherm, which impacts analyses of lower mantle velocities and composition.

1. Introduction

One of the grand challenges in geophysics is to resolve the thermal structure of the Earth's interior. This is clearly not an isolated problem but a fundamental one to clarify the dynamics, evolution, and chemical stratification of the planet [Murakami *et al.*, 2012]. Besides, a one dimensional (1D) temperature profile is an abstract construct – a spherically averaged reference temperature model consistent with spherically averaged velocity and composition profiles. To date, numerous one dimensional temperature profiles, or geotherms, have been suggested and calculated by various means and using different assumptions. For example, these include: seismological observations [Brown and Shankland, 1981], geochemical input [Anderson, 1982; Anzellini *et al.*, 2013; Boehler, 2000], mineral physics computations [da Silva *et al.*, 2000; Karki *et al.*, 2001; Wang *et al.*, 2015] or measurements [Stixrude and Lithgow-Bertelloni, 2011], geodynamic simulations [Matyska and Yuen, 2002], or a combination of them [Hernlund *et al.*, 2005]. Differences between them arise not only from the technique or input data, but from the constraints to which they are subjected to, i.e., the melting temperature of iron, phase transitions, seismic discontinuities, convection processes, and lower mantle composition. In addition, lateral velocity heterogeneities point to lateral temperature and/or composition variations, a very difficult problem that still awaits, e.g., advances in geodynamic simulations. Thus, construction of one dimensional temperature profiles must be seen as an insufficient but a necessary exercise to advance this topic.

An essential aspect in constructing a geotherm, is to define a suitable potential temperature, i.e., the boundary condition for integration of the adiabatic gradient. Most

geotherms are anchored to depths associated with seismic discontinuities (e.g. the ~ 660 km discontinuity), where phase transitions occur [Poirier, 2000]. For the top of the lower mantle, we assumed a temperature of 1873K at 23GPa as in *Brown and Shankland* [1981] (B&S) (See also [Akaogi and Akimoto, 1979]). The latter is an adiabatic temperature profile constructed from the Debye entropy formulation [Brillouin, 1953] and the acoustic velocities from the preliminary reference Earth model (PREM) [Dziewonski and Anderson, 1981]. This geotherm is considered by many to be the standard adiabatic geotherm for the lower mantle. It's important to point out that the conditions at which ringwoodite dissociates into bdg and fp are still somewhat controversial [Irifune et al., 1998; Chudinovskikh and Boehler, 2001; Katsura et al., 2001]. Thus, the appropriate potential temperature for the lower mantle geotherm is debatable. Several other geotherms, e.g., *Anderson* [1982], *Boehler* [2000] and *Anzellini et al.* [2013] were obtained by extrapolating the temperature from the inner and outer core geotherm using the phase diagram of iron. Additionally, geotherms constructed from first- principles include different approaches; for instance, *da Silva et al.* [2000] and *Karki et al.* [2001] calculated the temperatures needed to fit the bulk modulus of pyrolite to PREM. Others such as *Tsuchiya et al.* [2016], constructed the geotherm from the set of temperatures of different isobars at which the vibrational entropy of bridgmanite was constant.

In this work, we integrated the isentropic gradient formula using thermodynamics properties of minerals obtained by first principles calculations, starting from the standard boundary condition at 660 km depth, i.e., the experimentally determined post-spinel transition conditions [Akaogi and Akimoto, 1979], also used by Brown and Shankland [Brown

and Shankland, 1981]. The relevant lower mantle phases are bridgmanite (Al-Fe-bearing MgSiO_3 perovskite) (bdg), CaSiO_3 perovskite (CaPv), and (Mg,Fe)O ferropericlasite (fp) [Irfune, 1994; Irfune et al., 2010; Murakami et al., 2012]. These minerals form a variety of aggregates commonly characterized by their Mg/Si molar ratio. However, the relative abundances of these aggregates in the lower mantle is still debatable [Irfune, 1994; Irfune et al., 2010; Murakami et al., 2012; Wu and Wentzcovitch, 2014; Wang et al., 2015; Wu, 2016]. Here we derived isentropes for likely mantle aggregates such as harzburgite (Mg/Si ~ 1.56) [Baker and Beckett, 1999], chondrite (Mg/Si ~ 1.07) [Hart and Zindler, 1986], pyrolite (Mg/Si ~ 1.24) [McDonough and Sun, 1995], peridotite (Mg/Si ~ 1.30) [Hirose and Kushiro, 1993], and perovskite only (Mg/Si ~ 0.82) [Williams and Knittle, 2005] to assess the effect of Mg/Si ratio on the isentrope. The presence of FeO in these aggregates needs special consideration. It is well known that ferrous iron (Fe^{+2}) in fp exhibits a spin crossover at lower mantle conditions [Badro et al., 2003; Speziale et al., 2005; Tsuchiya et al., 2006], which introduces anomalies in its thermodynamics [Wentzcovitch et al., 2009; Wu et al., 2009] and thermoelastic properties [Crowhurst et al., 2008; Marquardt et al., 2009; Antonangeli et al., 2011; Murakami et al., 2012; Wu et al., 2013; Wu and Wentzcovitch, 2014]. Here we investigated in details how these anomalies affect the isentropes of these aggregates in the lower mantle. We compare the temperature gradients of aggregates with iron in fp in the high spin (HS) state and iron undergoing the spin crossover, i.e., in a mixed spin state (MS) of HS and low spin (LS). Clarification of the effect of this spin crossover in the isentropes of several aggregates is a first order question in advancing

the problem of mantle temperatures. Finally, we examined the effect such spin crossover induced thermal anomalies have on aggregate velocities.

2. Method and Calculation Details

The thermoelastic properties of bdg $\text{Mg}_{1-x}\text{Fe}_x\text{SiO}_3$ ($x = 0$ and 0.125) and fp $\text{Mg}_{1-y}\text{Fe}_y\text{O}$ ($y = 0$ and 0.1875) were obtained from *Shukla et al.* [2015a] and *Wu et al.* [2013] respectively. Results for other x and y concentrations shown in this work were linearly interpolated and only high spin (HS) Fe^{2+} -bdg was used since no spin crossover in Fe^{2+} occurs in bdg at lower mantle conditions [*Bengtson et al.*, 2009; *Hsu et al.*, 2010; *Hsu and Wentzcovitch*, 2014; *Shukla et al.*, 2015a, b; *Lin et al.*, 2016]. For CaPv, thermoelastic properties from *Kawai and Tsuchiya* [2014] were reproduced within the Mie-Debye-Grüneisen [*Stixrude and Lithgow-Bertelloni*, 2005] formalism (see Supporting Information).

We considered mixtures of SiO_2 - MgO - CaO - FeO for relevant mantle aggregates; namely, harzburgite [*Baker and Beckett*, 1999], chondrite [*Hart and Zindler*, 1986], pyrolyte [*McDonough and Sun*, 1995], peridotite [*Hirose and Kushiro*, 1993], and perovskitic only [*Williams and Knittle*, 2005]. We imposed a fixed iron partitioning coefficient $K_D = \frac{x/(1-x)}{y/(1-y)}$ between bdg and fp of 0.5 [*Irifune et al.*, 2010]. This assumption is not questioned in the present work, but should be further investigated theoretically in the future. Also, the effect of Al_2O_3 was not assessed here. Instead, its moles were equally distributed between SiO_2 and MgO to keep the Mg/Si molar ratio almost unchanged. We show in Tables S1 and S2 the weight, molar, and volume percentages of oxides and minerals in the aggregates considered.

The isentropes of different minerals and aggregates were found from their isentropic gradients computed as,

$$\left(\frac{\partial T}{\partial P}\right)_S = \frac{\alpha_{agg} V_{agg} T}{C_{p_{agg}}} \quad (1)$$

where the aggregate quantities $V_{agg} = \sum_i \phi_i V_i$, $\alpha_{agg} = \sum_i \alpha_i \phi_i V_i / V_{agg}$, and $C_{p_{agg}} = \sum_i \phi_i C_{p_i}$ are the molar volume, thermal expansion coefficient, and isobaric specific heat, respectively. Here, ϕ_i , V_i , α_i , and C_{p_i} represent respectively the molar fraction, molar volume, thermal expansion coefficient, and isobaric specific heat of the i^{th} mineral in the mixture. All the isentropes, here loosely referred as geotherms, were compared with the adiabatic [*Brown and Shankland, 1981*] and superadiabatic [*Anderson, 1982*] geotherms. Once these geotherms are obtained, we compute aggregate velocities along aggregate specific geotherms using the Voigt-Reuss-Hill (VRH) average of elastic moduli and compared with PREM values [*Dziewonski and Anderson, 1981*].

3. Results and Discussion

3.1. Lower mantle mineral isentropes

To unravel the possible consequences of the iron spin crossover in fp on the lower mantle geotherm, first we calculated using Eq.1, the isentropes of $(\text{Mg}_{0.875}\text{Fe}_{0.125})\text{SiO}_3$, CaSiO_3 , and $(\text{Mg}_{0.8125}\text{Fe}_{0.1875})\text{O}$ with iron in HS and MS states (See Figure 1). Here, differences between $(\text{Mg}_{0.875}\text{Fe}_{0.125})\text{SiO}_3$ and CaSiO_3 are only noticeable at higher pressures, and no sudden changes in the slopes of such isentropes were observed (See Figure 1a). For fp however, the isentropes of MS and HS states differ by ~ 260 K at deep lower mantle pressures (Figure 1a). The anomalies caused by the spin crossover on V , α , and C_p (See

Figures 1b to 1d) on the adiabatic gradient of fp (Figure 1e) are responsible for such temperature increase. Note that for α and C_p , the spin crossover anomalies correspond to broad peaks at similar pressure ranges, but do not cancel during the adiabatic gradient integration owing to significant differences in their magnitudes (Figures 1c and 1d).

3.2. Effect of Mg/Si ratio fp spin crossover on the geotherm

We now investigate the isentropes of aggregates likely to be present in the lower mantle. Their compositions are shown in Figure 2. The horizontal charts in Figure 2a represent the oxides mol% of SiO₂ - MgO - CaO FeO in the aggregate, while the pie charts in Figure 2b show the mol% of each mineral (bdg,fp,CaPv) in the aggregate. Each composition is characterized by its Mg/Si molar ratio, and it is clear that as Mg/Si decreases, so does the amount of fp. Further details about these compositions can be found in the Supporting Information.

Al₂O₃ and Fe₂O₃ were not regarded here and their inclusion in the lower mantle mixture is important to fully discern the lower mantle thermal behavior and composition. However, due to the presumptive low ferric iron concentration in the lower mantle ($\text{Fe}^{3+}/\Sigma\text{Fe} \sim 0.01-0.07$) [Xu *et al.*, 2015], the spin crossover effect in the $(\text{Mg}_{1-y}\text{Fe}_y^{3+})(\text{Si}_{1-y}\text{Fe}_y^{3+})\text{O}_3$ thermodynamic properties and thus the isentrope is negligible [Shukla and Wentzcovitch, 2016]. Also, it was recently shown by Shukla *et al.* [2016] that the thermodynamic and thermoelastic properties of $(\text{Mg}_{1-y}\text{Fe}_y^{3+})(\text{Si}_{1-y}\text{Al}_y)\text{O}_3$ are very similar to those of $(\text{Mg}_{1-x}\text{Fe}_x^{2+})\text{SiO}_3$, and therefore, the results shown here should not vary significantly. However, the contribution of CaO was not ignored as is usually done in the literature [Wentzcovitch *et al.*, 2004; Murakami *et al.*, 2012; Wang *et al.*, 2015] due to its relatively

small abundance in the lower mantle. The thermoelastic properties of CaPv obtained by *Stixrude and Lithgow-Bertelloni* [2011] and *Kawai and Tsuchiya* [2015] are quite significant (Figures S5 and S7). The smaller shear modulus of *Kawai and Tsuchiya* [2015] helps to reduce discrepancies with PREM values for all aggregates containing CaPv.

We first examined the temperature increments caused by the spin crossover in all aggregates in which fp does (MS) and does not (HS) undergo spin crossover (Figure 3). Adiabatic geotherms and gradients (insets) for harzburgite, peridotite, pyrolite, and chondrite are shown in Figures 3a to 3d. The temperature differences between HS and MS at high pressures ($P \sim 125\text{GPa}$) for harzburgite ($\sim 50\text{ K}$) were greater than those for peridotite ($\sim 40\text{ K}$), pyrolite ($\sim 30\text{ K}$), and chondrite ($\sim 20\text{ K}$) owing to harzburgite's higher Mg/Si. We also notice that MS gradients (insets) for all aggregates deviate from HS at pressures of $\sim 60\text{ GPa}$, as a consequence of the spin crossover, and the gradient decreases in proportion to the Mg/Si ratio.

The isentropes of all aggregates are compared with reference geotherms by *Brown and Shankland* [1981] and *Anderson* [1982] in Figure 4. All calculated adiabats were anchored to 1873K at 23GPa as in *Akaogi and Akimoto* [1979] and *Brown and Shankland* [1981]. At deep lower mantle conditions, harzburgite achieves the highest temperature, which is about $\sim 200\text{ K}$ higher than that of B&S. Temperatures then decrease with respect to the Mg/Si ratio, i.e., the aggregate's fp fraction.

4. Geophysical Significance

The elastic moduli (K_S, G), acoustic velocities (V_P, V_ϕ, V_S), and densities (ρ) of all the aggregates along their own isentropes are shown in Figure 5. In aggregates containing

fp, K_S softening due fp spin crossover [Wu *et al.*, 2013; Wu and Wentzcovitch, 2014] is observed and varies proportionally to the Mg/Si ratio (Figure 5a). Moreover, G does not exhibit any anomalous behavior and its value for different compositions converges to similar values at deep lower mantle pressures. For aggregates with higher Mg/Si ratio, calculated G revealed a better agreement with PREM values, while the K_S values for chondrite and pyrolite were closer to PREM values (Figure 5a). The signature of K_S anomalies were also obvious in the compressional ($V_p = \sqrt{(K_S + \frac{4}{3}G)/\rho}$) and bulk ($V_\phi = \sqrt{K_S/\rho}$) velocities, while shear velocities $V_S = \sqrt{G/\rho}$ were unaffected (See Figure 5b).

The relative velocity deviations (ΔV_P , ΔV_ϕ , and ΔV_S) from PREM values are shown in Figure 5c. ΔV_P and ΔV_ϕ decreased with increasing Mg/Si ratio, and reached negative values mainly due fp spin crossover. However, ΔV_S for all the aggregates was positive and the deviations from PREM values for peridotite and harzburgite were the lowest. The relative density deviations ($\Delta\rho$) reduced with increasing pressure (Figure 5c). For compositions with fp, the volume collapse caused by fp spin crossover [Wentzcovitch *et al.*, 2009] seemed to reduce such deviations further.

Moreover, as discussed in section 3.2, the iron spin crossover in fp raises the aggregate's geotherm in proportion to its fp content (or to the iron content in fp). This temperature boost can affect analyses of the lower mantle composition. Figures 6a and 6a' show peridotite and pyrolite's elastic moduli along their own geotherms and the B&S geotherm. Although not substantial, relative deviations from PREM varied depending on the geotherm used. For the bulk modulus ΔK_S in Figures 6b and 6b', the relative deviations from PREM were the same along both geotherms until pressures lower than 80

GPa, while for the shear modulus relative deviations ΔG , results along the self-consistent geotherm (Figures 6c and 6c') exhibited lower deviations from PREM throughout the whole lower mantle. Such details suggest that the aggregate thermoelastic properties along the self-consistent geotherm should sharpen uncertainties in analyses of lower mantle composition.

5. Conclusions

We presented a set of adiabatic geotherms for individual minerals and likely lower mantle aggregates under realistic conditions. We showed that the spin crossover in ferropericlase introduces an anomaly in its isentrope similar to “superadiabaticity”. This effect increases the adiabatic temperature gradient in different aggregates in proportion to their ferropericlase content or Mg/Si ratio. Velocities of aggregates with compositions varying from perovskitic to harzburgitic along their self-consistent geotherms exhibited deviations from PREM velocities within $\pm \sim 2\%$. However, pyrolitic and peridotitic compositions displayed the best fit with respect to PREM values. The elastic moduli, velocities, and densities of these aggregates along their own self-consistent geotherms tend to display smaller deviations from PREM (up to $\sim 1\%$ less), than those along standard geotherms such as *Brown and Shankland* [1981]. We stress here that we cannot afford to ignore the impact from the spin crossover anomalies, because neglecting them would lead to erroneous interpretations of the lower mantle geotherm and composition.

Acknowledgments. The authors acknowledge Caroline Qian for her early contributions to the isentrope code. This work was supported primarily by grants NSF/EAR 1319368, 1348066, and NSF/CAREER 1151738. Zhongqing Wu was supported by State

Key Development Program of Basic Research of China (2014CB845905) and NSF of China (41274087). C. Houser was supported by the Earth-Life Science Institute at Tokyo Institute of Technology. Results produced in this study are available in the supporting information.

6. Supplementary Material

Introduction

The supporting information consists of Texts S1-S4, Figures S1-S7, and Tables S1-S4. Figure S1 shows properties of pyrolite (V , α , and C_p) with fp in HS and MS states.

Elastic moduli and acoustic velocities for the different aggregates are shown in Figures S2 to S4. Figure S5 shows the isentropes for CaSiO_3 using MDG parameters from *Stixrude and Lithgow-Bertelloni* [2011] and *Kawai and Tsuchiya* [2014]. Figure S6 shows the elastic constants of CaPv reported by *Kawai and Tsuchiya* [2015] fitted to a Mie-Debye-Grüneisen model. Figure S7 depicts the compression curves and moduli of CaPV using *Stixrude and Lithgow-Bertelloni* [2011] and *Kawai and Tsuchiya* [2014, 2015] MDG parameters. Texts S1-S3 are supporting analyses of what is presented in Figures S1-S7.

Table S1 shows the mol% and wt% of the oxides of each of the aggregates considered. It also shows how the compositions were before the Al_2O_3 moles were adjusted. Table S2 shows the mol%, vol%, and wt% of each of the minerals in all the aggregates, along with the Fe concentrations in bdg and fp (x and y). Tables S3 and S4 shows the adiabats for the minerals and aggregates studied.

Text S1. We compared the pyrolite's adiabat properties when its fp (30 mol% in pyrolite) did (MS) and did not (HS) undergo spin transition. Figure S1 shows pyrolite's α , C_p and

V calculated along its own geotherm. Compression curves differences are subtle (Figure S1a), while the anomalies introduced in α and C_p (Figures S1b and S1c respectively) cause broad peaks throughout the spin crossover at equivalent pressure ranges.

Text S2. Elastic moduli, velocities and densities of the minerals in each aggregate, calculated along the aggregate geotherm, can be found in Figures S2, S3, and S4. It can be observed that K_S for bdg and CaPv behave similarly, but CaPv shear modulus G is significantly smaller than that of bdg. In all aggregates, K_S for both perovskites is larger than PREM values. G for bdg displays values greater than PREM, while CaPv G agrees well until mid lower mantle pressures, and then deviates to values smaller than those of PREM. Finally, moduli for fp are always smaller than PREM values and showed clear anomalies associated with spin crossover. The velocities followed a trend consistent with that of the moduli, while for the densities we observed that CaPv is denser than bdg. Also, fp increases its density at mid lower mantle pressures due the volume collapse caused by the spin crossover.

Text S3. Isentropes for CaPv were calculated using *Stixrude and Lithgow-Bertelloni* [2011] MDG parameters, which are different from those obtained by *Kawai and Tsuchiya* [2014] (See Figure S5). They differ by $\sim 200\text{K}$ in the deep lower mantle. Therefore, the thermodynamic model adopted for CaPv has some influence on the geotherm.

We used CaPv properties reported by *Kawai and Tsuchiya* [2014, 2015] for all the aggregates. Figure S6 shows the elastic constants of CaPv for different isotherms, while Figures S7a and S7b compare compression curves and moduli between *Stixrude and Lithgow-Bertelloni* [2011] and *Kawai and Tsuchiya* [2014, 2015].

References

- Akaogi M. and Akimoto S. (1979), High-pressure phase equilibria in a garnet lherzolite, with special reference to Mg^{2+} Fe^{2+} partitioning among constituent minerals, *PEPI*, *19*, 31–51.
- Anderson O. L. (1982), The Earth's core and phase diagram of iron, *Phil. Trans. R. Soc. Lond. A*, *306*, 21–35.
- Antonangeli D., Siebert J., Aracne C.M., Farber D.L., Bosak A., Hoesch M., Krisch M., Ryerson F.J., Fiquet G. and Badro J. (2011), Spin crossover in ferropericlase at high pressure: a seismologically transparent transition?, *Science*, *331*, 64-67.
- Anzellini, S., Dewaele, A., Mezouar, M., Loubeyre, P., and Morard, G. (2013), Melting of iron at Earth's inner core boundary based on fast X-ray diffraction, *Science*, *340*, 464-466.
- Badro J., Fiquet G., Guyot F., Rueff J.P., Struzhkin V.V., Vank G. and Monaco G. (2003), Iron partitioning in Earth's mantle: toward a deep lower mantle discontinuity, *Science*, *300*, 789-791.
- Baker M.B., J.R. Beckett (1999), The origin of abyssal peridotites: a reinterpretation of constraints based on primary bulk compositions, *Earth Planet. Sci. Lett.*, *171*, 49-61.
- Bengtson A., Li J., and Morgan D. (2009), Mössbauer modeling to interpret the spin state of iron in (Mg, Fe) SiO_3 perovskite, *Geophys. Res. Lett.*, *36*, L15301, doi:10.29/2009GL038340.
- Boehler R. (2000), High-pressure experiments and the phase diagram of lower mantle and core materials, *Rev. Geophys.*, *2*, 221–245, doi:10.1029/1998RG000053.

Brillouin, L. (1953), Wave propagation in periodic structures: electric filters and crystal lattices, *Dover Publications, Inc., 2nd Edition*.

Brown J.M. and T.J. Shankland (1981), Thermodynamic parameters in the Earth as determined from seismic profiles, *Geophys. J. R. astr. Soc.*, *66*, 579–596.

Chudinovskikh, L., and Boehler, R. (2001), High-pressure polymorphs of olivine and the 660-km seismic discontinuity, *Nature*, *411*, 574–577.

Crowhurst, J.C., Brown, J.M., Goncharov, A.F. and Jacobsen, S.D. (2008), Elasticity of (Mg, Fe) O through the spin transition of iron in the lower mantle, *Science*, *319*, 451–453.

da Silva C.R.S., R.M. Wentzcovitch, A. Patel, G.D. Price, S.I. Karato (2000), The composition and geotherm of the lower mantle: constraints from the elasticity of silicate perovskite, *Phys. Earth Planet. Int.*, *118*, 103–109.

Dziewonski, A. M., and D. L. Anderson (1981), Preliminary reference Earth model, *Phys. Earth Planet. Int.*, *25*, 297–356.

Hart S. R. and A. Zindler (1986), In search of a bulk-Earth composition, *Chem. Geo.*, *57*, 247–267, doi:10.1016/0009-2541(86)90053-7.

Hernlund J. W., Thomas, C., and Tackley, P. J. (2005), A doubling of the post-perovskite phase boundary and structure of the Earth's lowermost mantle, *Nature*, *434*, 882–886.

Hirose K. and I. Kushiro(1993), Partial melting of dry peridotites at high pressures: Determination of compositions of melts segregated from peridotite using aggregates of diamond, *EPSL*, *114*, 477–489.

Hsu H., Umemoto K., Blaha P., and Wentzcovitch R.M. (2010), Spin states and hyperfine interactions of iron in (Mg,Fe)SiO₃ perovskite under pressure *EPSL*, *294*, 19-26.

Hsu H. and R. M. Wentzcovitch (2014), First-principles study of intermediate-spin ferrous iron in the Earth's lower mantle, *Phys. Rev. B*, *90*, 195205, doi:10.1103/PhysRevB.90.195205.

Irifune T., T. Shinmei, C. A. McCammon, N. Miyajima, D. C. Rubie, D. J. Frost (2010), Iron partitioning and density changes of pyrolite in Earth's lower mantle, *Science*, *327*, 193–195.

Irifune T. (1994), Absence of an aluminous phase in the upper part of the Earth's mantle, *Nature*, *370* (1994), 131-133.

Irifune T., Nishiyama N., Kuroda K., Inoue T., Isshiki M., Utsumi W., Funakoshi K.I., Urakawa S., Uchida T., Katsura T. and Ohtaka O (1998), The postspinel phase boundary in Mg₂SiO₄ determined by in situ X-ray diffraction, *Science*, *279* (1998), 1698–1700.

Karki B., R. Wentzcovitch, S. de Gironcoli, S. Baroni (2001), First principles thermoelasticity of MgSiO₃-perovskite: consequences for the inferred properties of the lower mantle, *Geophys. Res. Lett.*, *28*, 26992702, doi:10.1029/2001GL012910.

Katsura T., Yamada H., Nishikawa O., Song M., Kubo A., Shinmei T., Yokoshi S., Aizawa Y., Yoshino T., Walter M.J., and Ito E. (2004), Olivine-wadsleyite transition in the system (Mg, Fe)₂SiO₄, *Geophys. Res. Solid Earth*, *109*, B02209, doi:10.1029/2003JB002438.

Kawai K. and T. Tsuchiya (2014), P-V-T equation of state of cubic CaSiO₃ perovskite from first-principles computation, *Geophys. Res. Solid Earth*, *119*, 28012809, doi:

10.1002/2013JB010905.

Kawai K. and T. Tsuchiya (2015), Small shear modulus of cubic CaSiO₃ perovskite, *Geophys. Res. Lett.*, *42*, 27182726, doi:110.1002/2015GL063446.

Lin J., Z. Mao, J. Yang, J. Liu, Y. Xiao, P. Chow, and T. Okuchi (2016), High-spin and Fe²⁺ and Fe³⁺ in single-crystal aluminous bridgmanite in the lower mantle, *Geophys. Res. Lett.*, *43*, 69526959, doi:10.1002/2016GL069836.

Marquardt H., Speziale S., Reichmann H.J., Frost D.J., Schilling F.R., and Garnero E.J. (2009), Elastic shear anisotropy of ferropericlase in Earth's lower mantle, *Science*, *324*, 224-226.

Matyska C., and Yuen, D. A. (2002), Bullens parameter η : a link between seismology and geodynamical modelling, *EPSL*, *198*, 471-483.

McDonough W.F., S.S. Sun (1995), The composition of the Earth, *Chem. Geo.*, *120*, 223-253, doi:10.1016/0009-2541(94)00140-4.

Murakami, M., Y. Ohishi, N. Hirao, and K. Hirose (2012), A perovskitic lower mantle inferred from high-pressure, high-temperature sound velocity data, *Nature*, *485*, 90–94, doi:10.1038/nature11004.

Poirier, J.P. (2000), Introduction to the Physics of Earth's Interior, *Cambridge Press*, *2nd Edition*.

Xu S., S.H. Shim, and D. Morgan (2015), Origin of Fe³⁺ in Fe-containing, Al-free mantle silicate perovskite, *Earth Planet. Sci. Lett.*, *409*, 319–328, doi:doi:10.1016/j.epsl.2014.11.006.

- Shukla, G., Z. Wu, H. Hsu, A. Floris, M. Cococcioni, and R. M. Wentzcovitch (2015a), Thermoelasticity of Fe²⁺-bearing bridgmanite, *Geophys. Res. Lett.*, *42*, 1741–1749.
- Shukla, G., M. Topsakal, and R. M. Wentzcovitch (2015b), Spin crossovers in iron-bearing MgSiO₃ and MgGeO₃: Their influence on the post-perovskite transition, *Phys. Earth Planet. Int.*, *249*, 11–17, doi:doi:10.1016/j.pepi.2015.10.002.
- Shukla, G., M. Cococcioni, and R. M. Wentzcovitch (2016), Thermoelasticity of Fe³⁺- and Al-bearing bridgmanite, *Geophys. Res. Lett.*, *43*, 56615670, doi:10.1002/2016GL069332.
- Shukla G. and R. M. Wentzcovitch (2016), Spin crossover in (Mg, Fe³⁺)(Si, Fe³⁺)O₃ bridgmanite: effects of disorder, iron concentration, and temperature, *Phys. Earth Planet. Int.*, Accepted, doi:doi:10.1016/j.pepi.2016.09.003.
- Speziale, S., A. Milner, V. E. Lee, S. M. Clark, M. P. Pasternak, and R. Jeanloz (2005), Iron spin transition in Earth's mantle, *Proc. Natl. Acad. Sci.*, *102*, 17918–17922.
- Stixrude, L. and C. Lithgow-Bertelloni (2005), Thermodynamics of mantle minerals I. Physical Properties, *Geophys. J. Int.*, *162*, 610–632.
- Stixrude, L. and C. Lithgow-Bertelloni (2011), Thermodynamics of mantle minerals II. Phase equilibria, *Geophys. J. Int.*, *184*, 1180–1213.
- Tsuchiya, T., Wentzcovitch, R. M., da Silva, C. R., and de Gironcoli, S. (2006). Spin transition in magnesiowstite in Earth's lower mantle, *Phys. Rev. Lett.*, *96*, 198501.
- Tsuchiya T., Kawai K., Wang X., Ichikawa H., and Dekura H. (2016), Temperature of the Lower Mantle and Core Based on Ab Initio Mineral Physics Data, *Deep Earth, John Wiley & Sons, Inc*, 13–30, doi:10.1002/9781118992487.

Wang X., T. Tsuchiya and A. Hase (2015), Computational support for a pyrolytic lower mantle containing ferric iron, *Nature Geoscience*, 8, 556-559, doi:10.1038/ngeo2458.

Wentzcovitch R. M., B. B. Karki, M. Cococcioni, and S. de Gironcoli (2004), Thermoelastic properties of MgSiO₃-Perovskite: Insights on the nature of the Earth's lower mantle, *Phys. Rev. Lett.*, 92, 018501, doi:10.1103/PhysRevLett.92.018501.

Wentzcovitch R. M., J. F. Justo, Z. Wu, C. R. S da Silva, A. Yuen, and D. Kohlstedt (2009), Anomalous compressibility of ferropericlase throughout the iron spin cross-over, *Proc. Natl. Acad. Sci.*, 106, 8447-8452.

Williams Q. and E. Knittle (2005), The Uncertain Major Element Bulk Composition of Earth's Mantle, *Earth's Deep Mantle: Structure, Composition, and Evolution. Geophysical Monograph Series 160. AGU*, doi:10.1029/160GM12.

Wu Z., J. F. Justo, and R. M. Wentzcovitch (2013), Elastic Anomalies in a Spin-Crossover System: Ferropericlase at Lower Mantle Conditions, *Phys. Rev. Lett.*, 110, 228501.

Wu Z., J. F. Justo, C. R. S da Silva, S de Gironcoli, and R. M. Wentzcovitch (2009), Anomalous thermodynamic properties in ferropericlase throughout its spin crossover transition, *Phys. Rev. B.*, 80, 014409.

Wu Z., and R. M. Wentzcovitch (2014), Spin crossover in ferropericlase and velocity heterogeneities in the lower mantle, *Proc. Natl. Acad. Sci.*, 111, 10468-10472.

Wu Z. (2016), Velocity structure and composition of the lower mantle with spin crossover in ferropericlase, *J. Geophys. Res. Solid Earth*, 121, 2304-2314, doi:10.1002/2015JB012667.

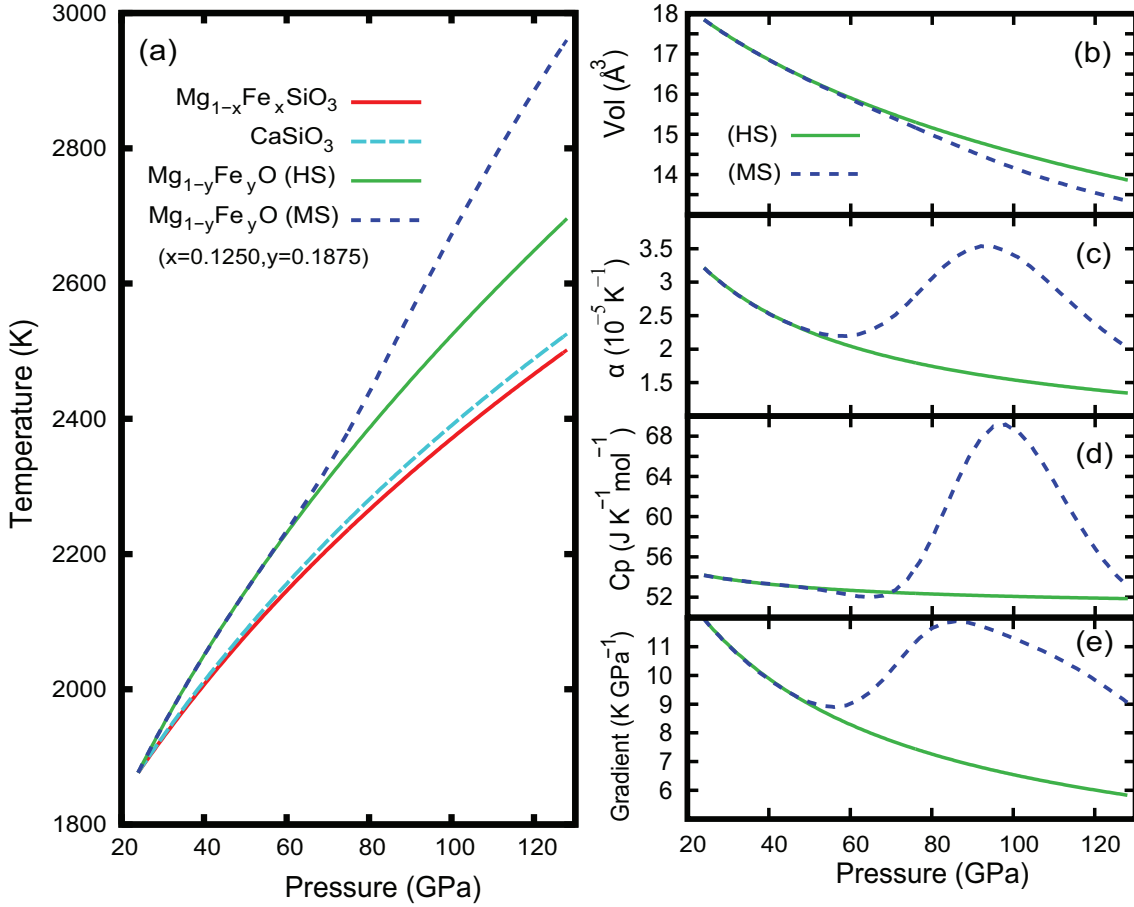


Figure 1. (a) Isentropes for bdg, CaPv, and fp in HS and MS states. (b) Volume, (c) thermal expansion coefficient (α), (d) isobaric specific heat (C_P), and (e) adiabatic gradient for fp in HS and MS states.

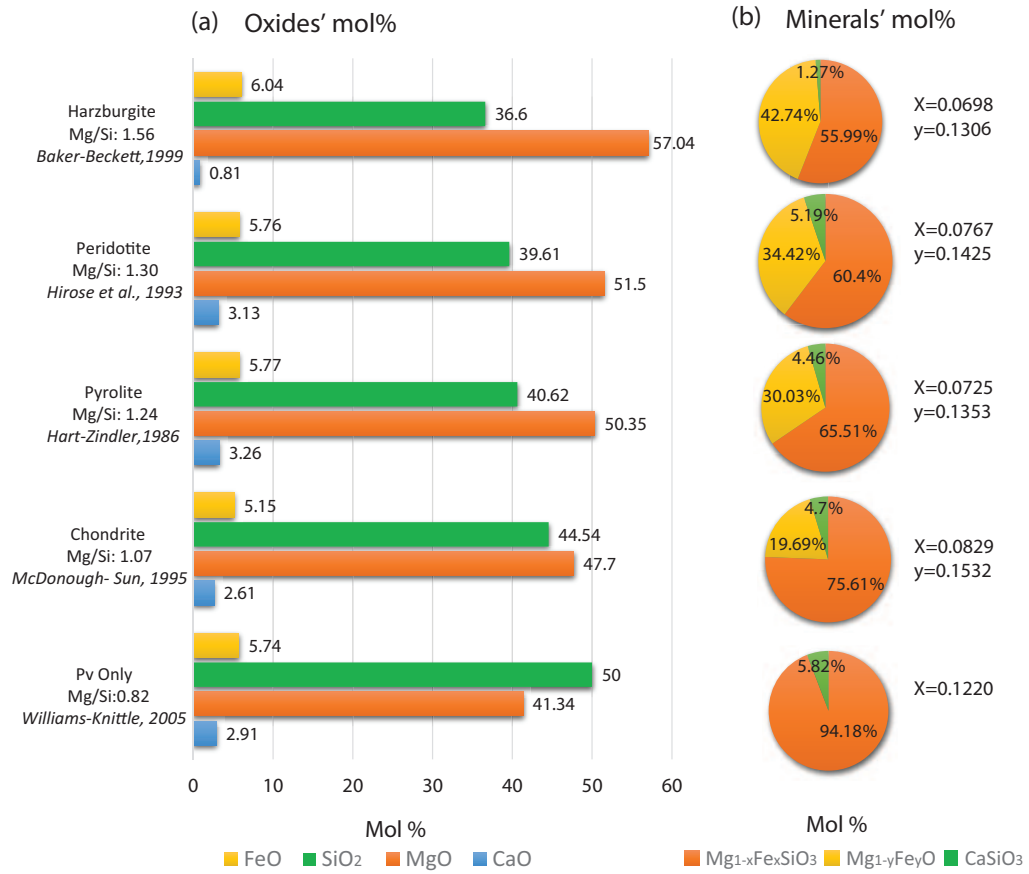


Figure 2. Aggregates characterized by their Mg/Si ratio. a) Mol% of oxides and b) minerals in each aggregate. The x and y values correspond to the molar fraction of iron in bdg and fp respectively.

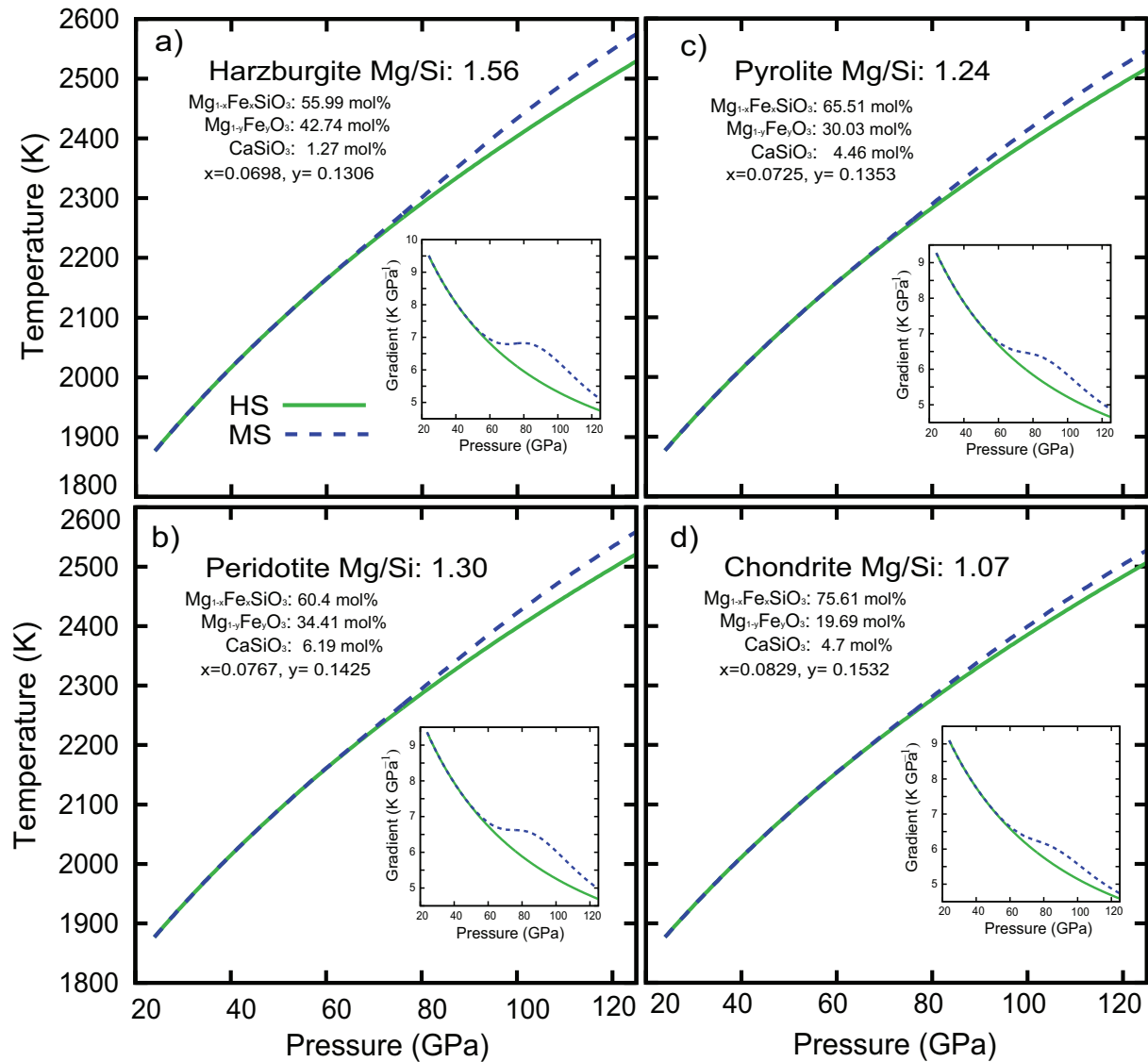


Figure 3. Adiabats for a) harzburgite, b) peridotite, c) pyrolite, and d) chondrite with fp in HS and MS states. The values of x and y correspond to the amount of iron in bdg and fp respectively. Solid/dashed lines correspond to adiabats with fp in HS/MS states. Inset figures show the adiabatic gradient for each aggregate.

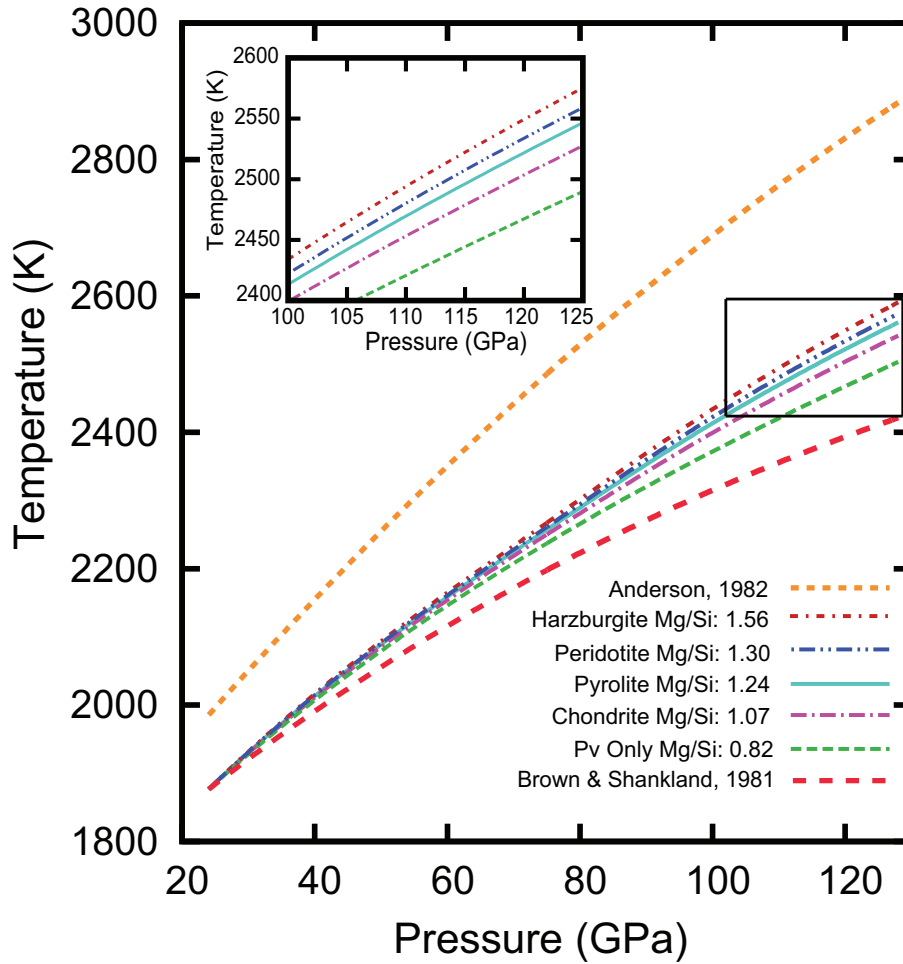


Figure 4. Calculated adiabats for aggregates considered, compared with geotherms by *Brown and Shankland* [1981] and *Anderson* [1982]. Inset corresponds to highlighted region.

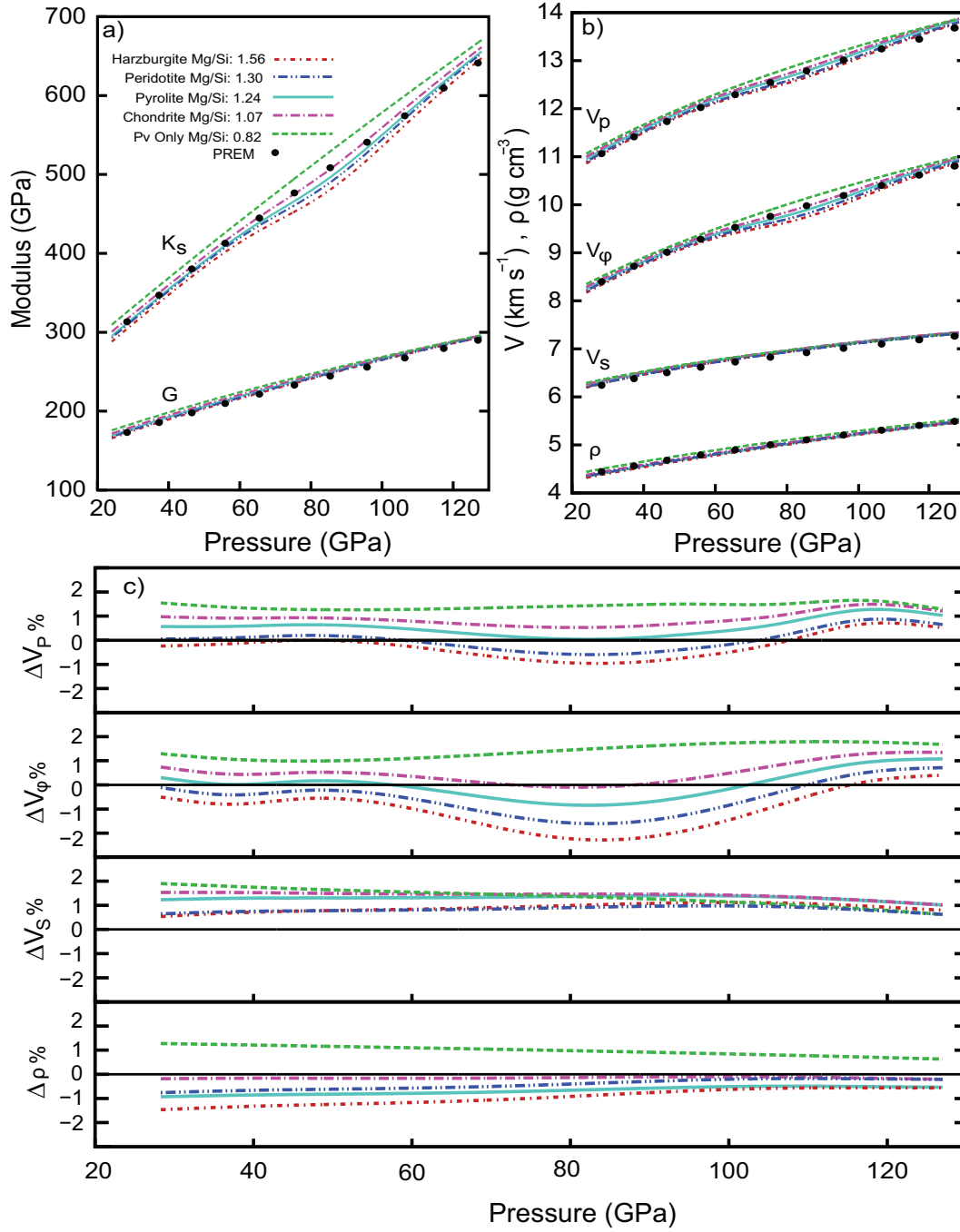


Figure 5. (a) Elastic moduli (K_S , G), (b) acoustic velocities (V_P , V_ϕ , V_S) and densities (ρ) for all aggregates considered. Black circles indicate PREM values [Dziewonski and Anderson, 1981]. (c) Relative deviations from PREM shown as percentages.

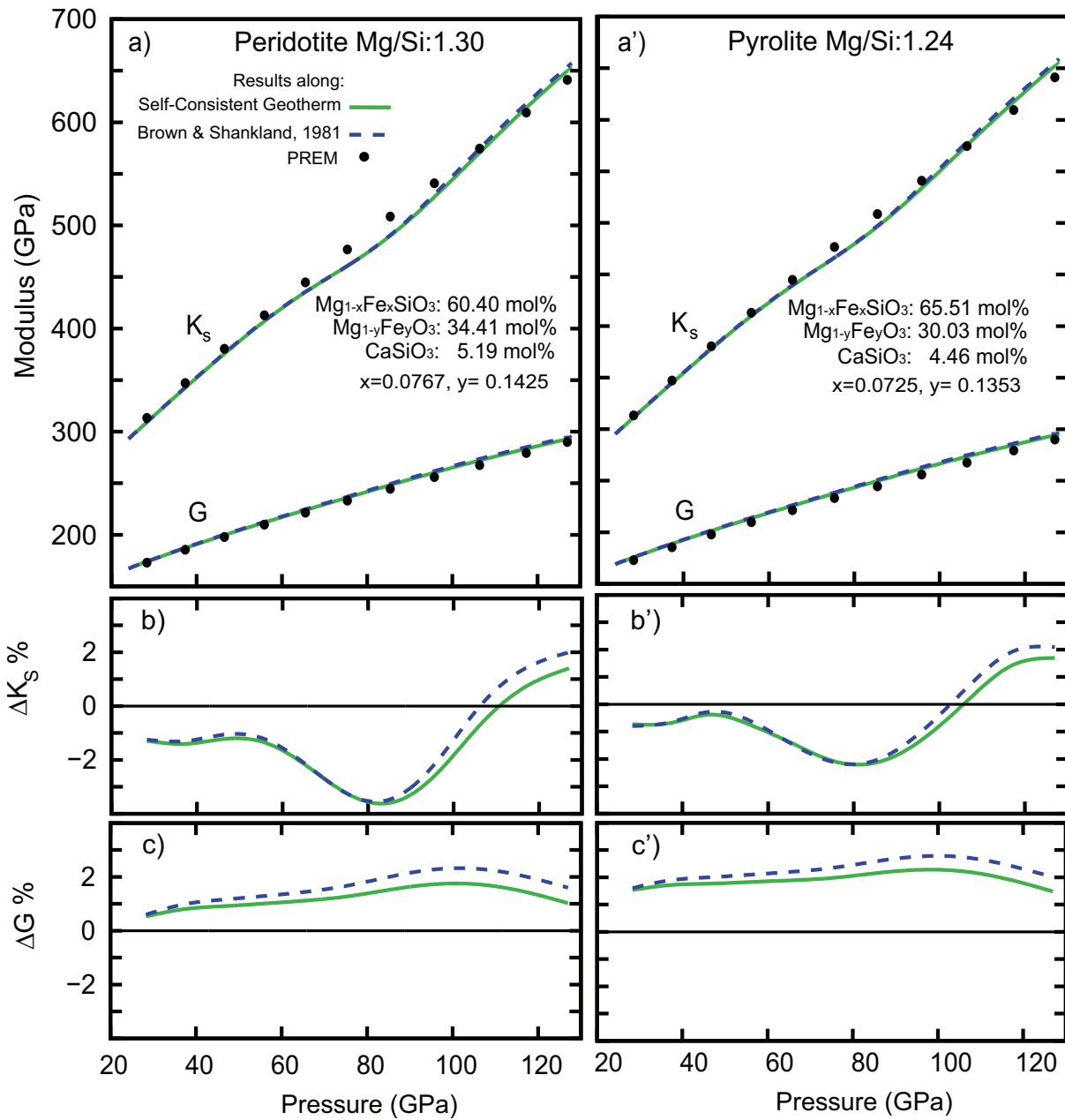


Figure 6. Elastic moduli (K_S , G) for (a) peridotite, and (a') pyrolite along self-consistent (solid green line) and *Brown and Shankland* [1981] (dashed blue line) geotherms. Black circles correspond to PREM values [*Dziewonski and Anderson, 1981*]. (b)/(b') and (c)/(c') are the elastic moduli relative deviations (ΔK_S , ΔG) with respect to PREM values, shown as percentages for peridotite/pyrolite.

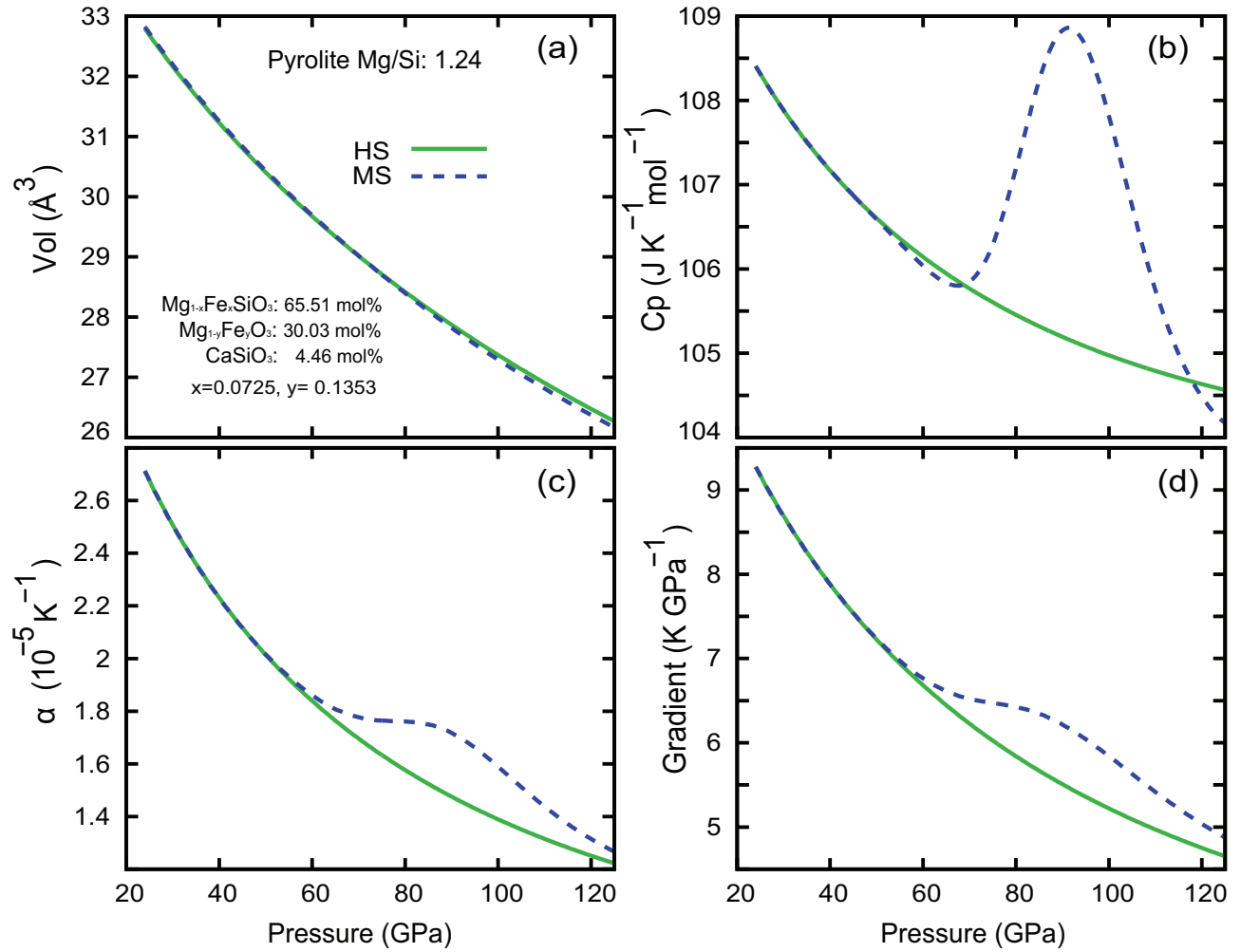


Figure S1. Properties of pyrolite with ferropericlasite in high spin state (HS) and mixed spin (MS) state along its own adiabat. (a) Volume, (b) thermal expansion coefficient, (c) isobaric specific heat and (d) adiabatic gradient.

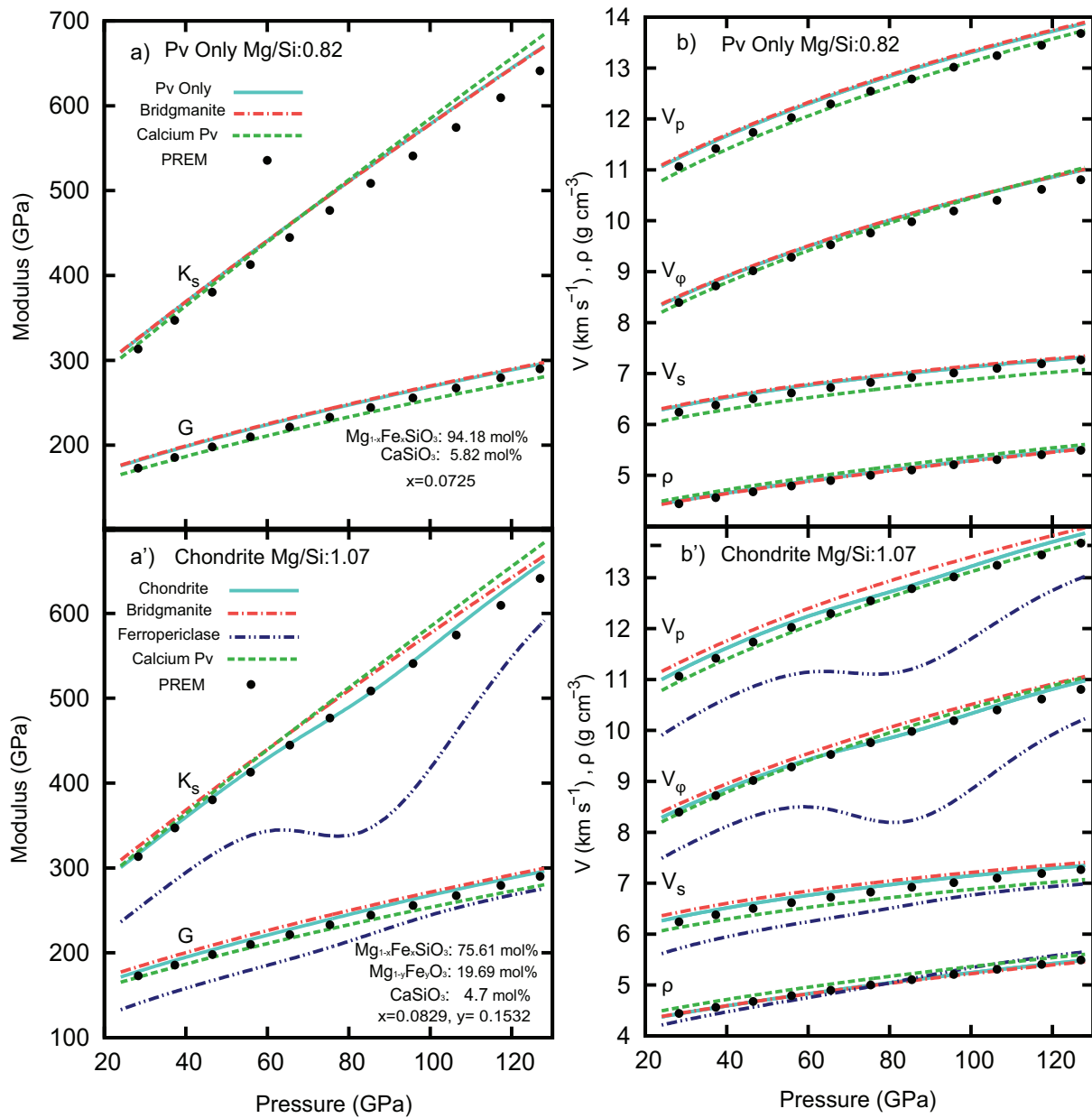


Figure S2. (a) and (a') are the elastic moduli (K_S , G) for Pv Only and chondritic aggregates respectively, while (b) and (b') are the acoustic velocities (V_P , V_ϕ , and V_S) and densities (ρ). The solid/dashed lines represent the aggregate/mineral properties.

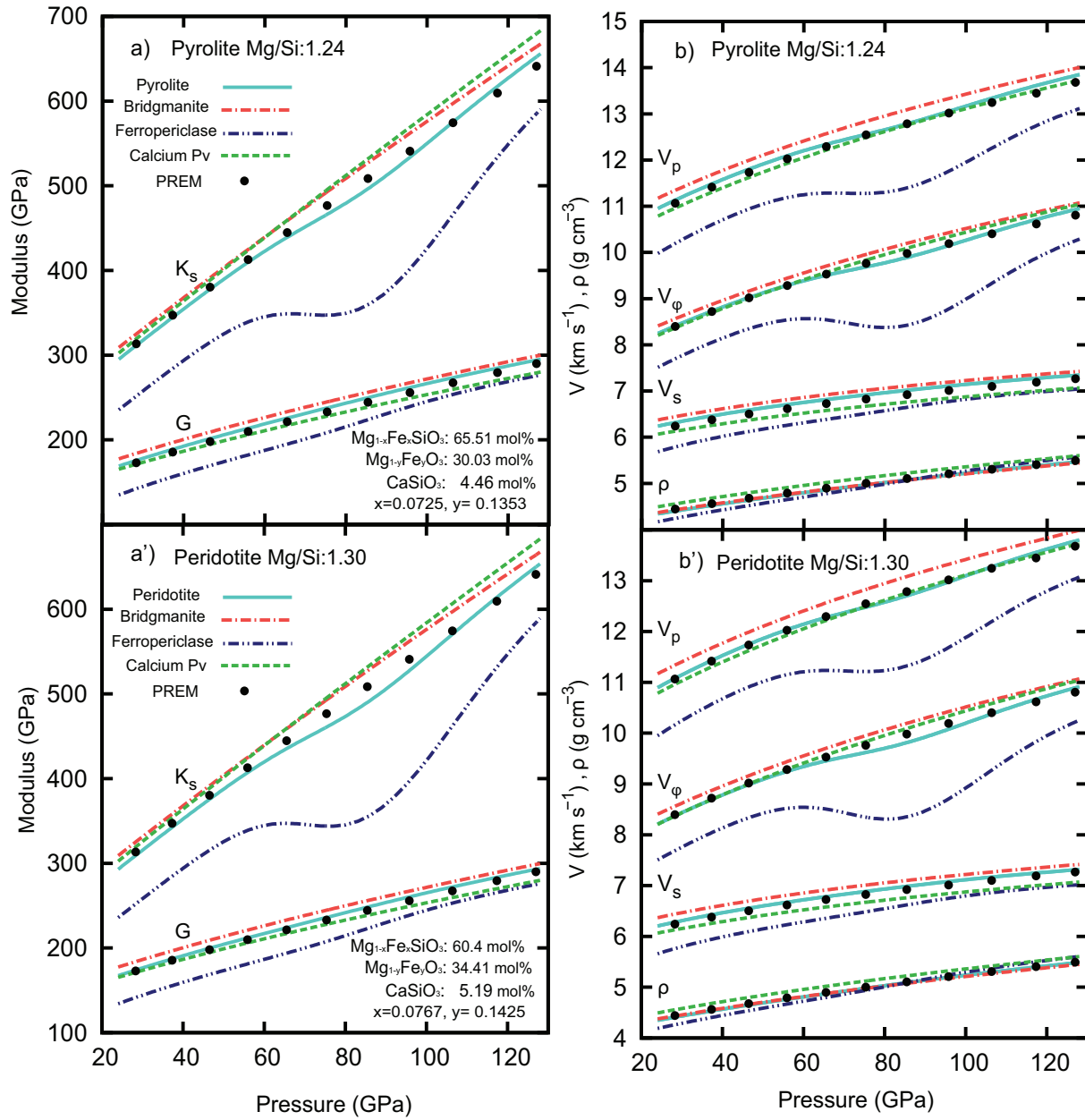


Figure S3. (a) and (a') are the elastic moduli (K_S , G) for pyrolite and peridotite compositions respectively, while (b) and (b') are the acoustic velocities (V_P , V_ϕ , and V_S) and densities (ρ). The solid/dashed lines represent the aggregate/mineral properties.

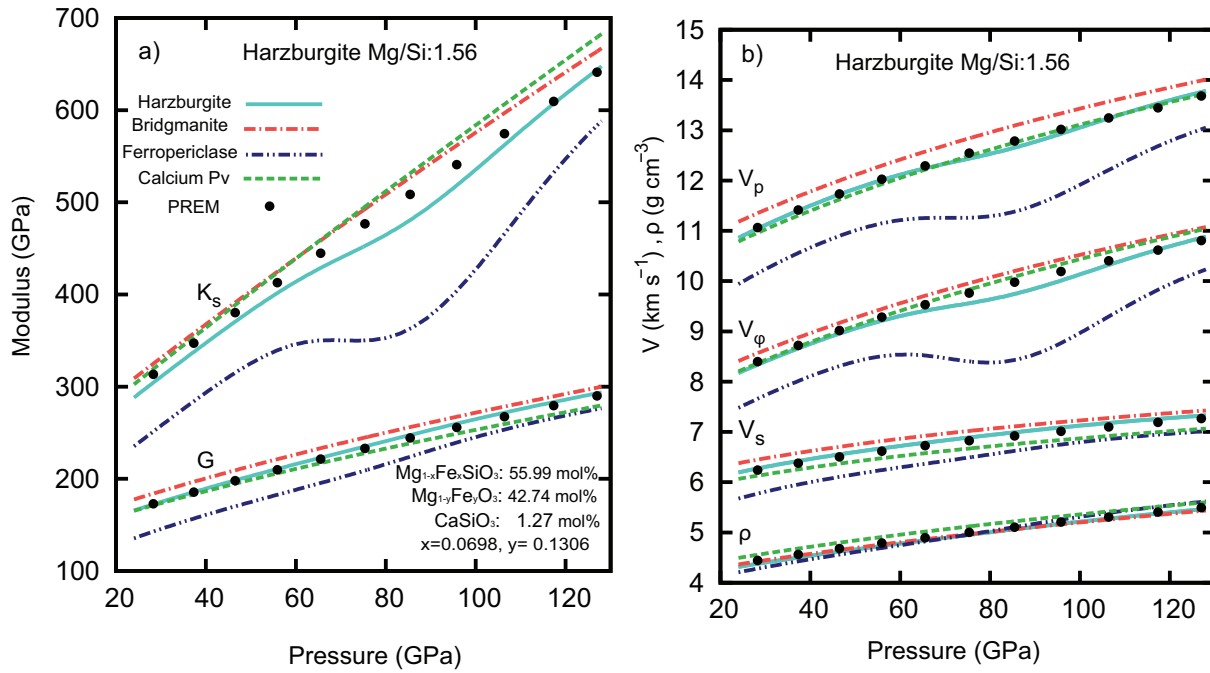


Figure S4. (a) Elastic moduli (K_S , G), (b) acoustic velocities (V_P , V_ϕ , and V_S), and densities (ρ) for harzburgite. The solid/dashed lines represent the aggregate/mineral properties

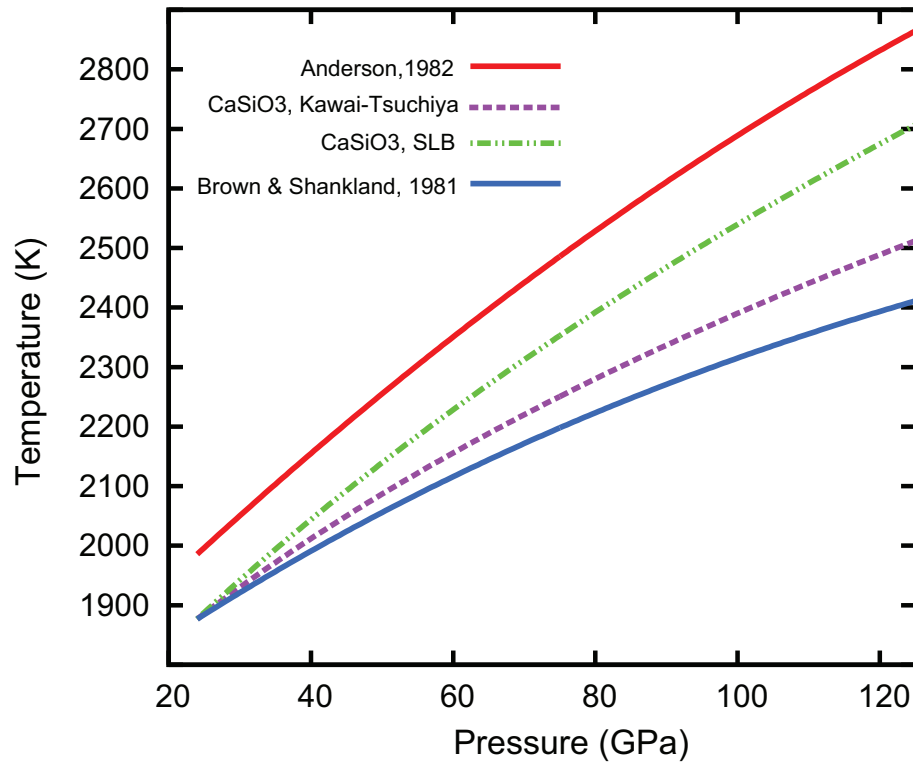


Figure S5. Calculated CaSiO_3 adiabats using MDG parameters from *Stixrude and Lithgow-Bertelloni* [2011] (SLB) and *Kawai and Tsuchiya* [2014]. At deep lower mantle pressures they differ by almost 200K

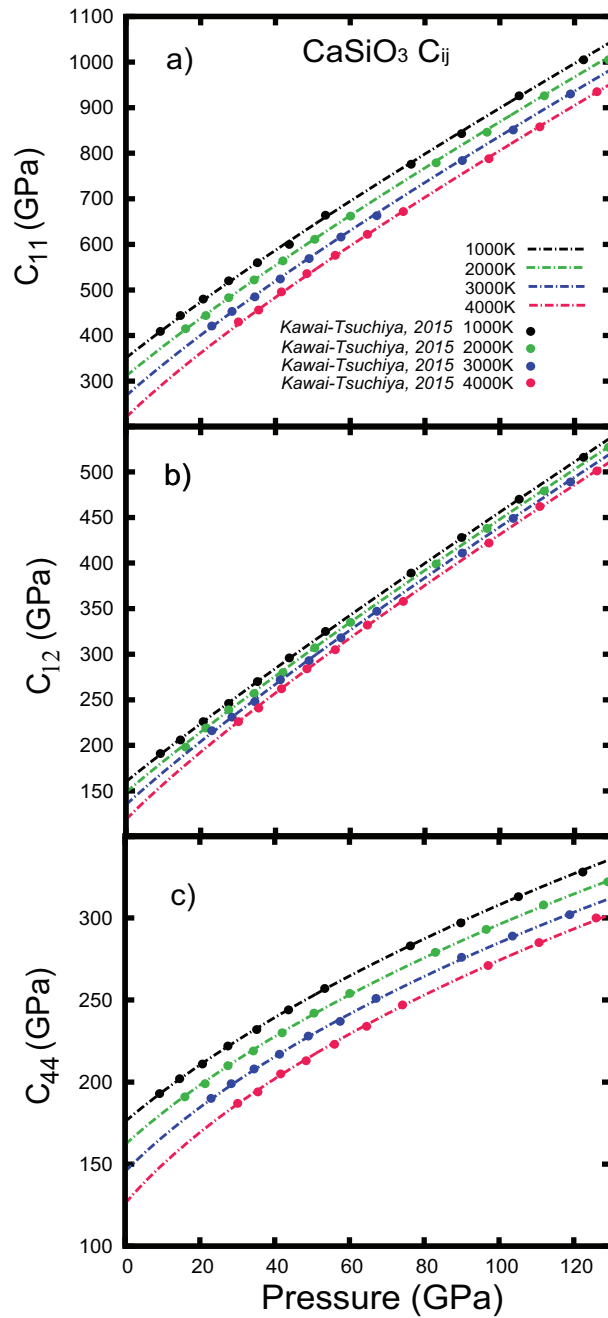


Figure S6. Results by *Kawai and Tsuchiya* [2015] fitted to a Mie-Debye-Grüneisen model developed in *Stixrude and Lithgow-Bertelloni* [2005] (See Eq. 2 in *Kawai and Tsuchiya* [2015])

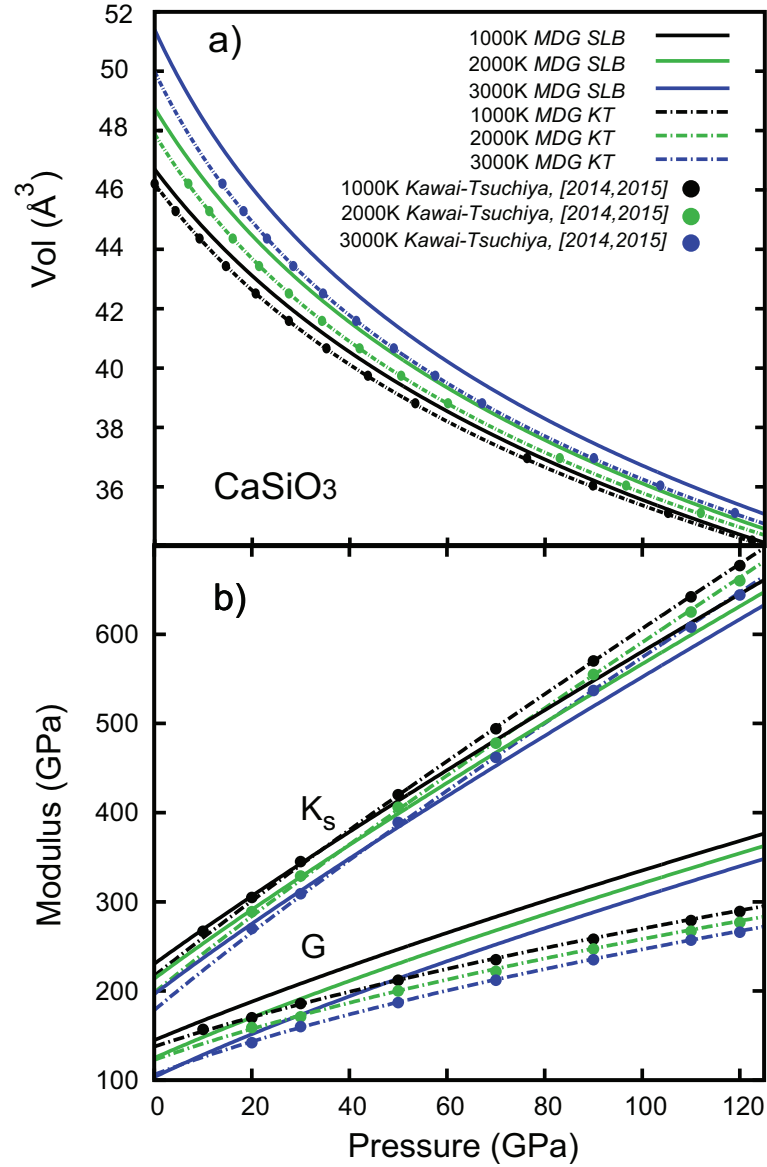


Figure S7. CaSiO_3 compression curves (a) and moduli (b) for different temperatures. Solid lines represent data obtained using the Mie-Debye-Grüneisen (MDG) model with EoS parameters from *Stixrude and Lithgow-Bertelloni* [2011] (SLB). Dashed lines are results calculated using parameters from *Kawai and Tsuchiya* [2014, 2015] (KW). Dots correspond to direct results reported by *Kawai and Tsuchiya* [2014, 2015].

Table 1. Fundamental oxides for lower mantle compositions. Bold data in brackets indicates original values before adjusting Al₂O₃ moles.

a *Williams and Knittle* [2005]

b *Hart and Zindler* [1986]

c *McDonough and Sun* [1995]

d *Hirose and Kushiro* [1993]

e *Baker and Beckett* [1999]

* MgO moles were further modified to avoid excess of this oxide

| | Perovskite ^a (Mg/Si: 0.82) Only | | Chondrite ^{a,b} (Mg/Si: 1.07) | | Pyrolite ^{a,c} (Mg/Si: 1.24) | | Peridotite ^d (Mg/Si: 1.30) | | Harzburgite ^e (Mg/Si: 1.56) | |
|--------------------------------|---|------------------------|--|------------------------|---------------------------------------|-----------------------|---------------------------------------|------------------------|--|------------------------|
| | Mol % | Wt % | Mol % | Wt % | Mol % | Wt % | Mol % | Wt % | Mol% | Wt % |
| CaO | 2.91 (2.89) | 3.11 (3) | 2.61 (2.65) | 2.86 (2.82) | 3.26 (3.33) | 3.61 (3.55) | 3.13 (3.19) | 3.48 (3.44) | 0.81 (0.81) | 0.91 (0.91) |
| MgO | 41.34* (41.79) | 31.76 (31.18) | 47.70 (46.74) | 37.59 (35.68) | 50.35 (49.3) | 40.05 (37.8) | 51.5 (50.61) | 41.14 (39.22) | 57.04 (56.51) | 46.17 (45.73) |
| SiO ₂ | 50 (47.50) | 57.26 (52.83) | 44.54 (43.52) | 52.32 (49.52) | 40.62 (39.37) | 48.17 (45) | 39.61 (38.50) | 47.17 (44.48) | 36.6 (36.07) | 44.16 (43.51) |
| FeO | 5.74 (5.70) | 7.86 (7.58) | 5.15 (5.25) | 7.24 (7.14) | 5.77 (5.89) | 8.18 (8.05) | 5.76 (5.86) | 8.2 (8.1) | 6.04 (6.07) | 8.76 (8.76) |
| Al ₂ O ₃ | (2.12) | (4) | (1.84) | (3.56) | (2.11) | (4.09) | (1.83) | (3.59) | (0.53) | (1.09) |

Table 2. Lower mantle minerals in different aggregates. The Vol % values are given at *Brown and Shankland*[1981] anchoring conditions.

| | Perovskite Only (Mg/Si: 0.82) $x = 0.1220$ | | | Chondritic (Mg/Si: 1.07) $x = 0.0829, y = 0.1532$ | | | Pyrolite (Mg/Si: 1.24) $x = 0.0725, y = 0.1353$ | | | Peridotite (Mg/Si: 1.30) $x = 0.0767, y = 0.1425$ | | | Harzburgite (Mg/Si: 1.56) $x = 0.0698, y = 0.1306$ | | |
|--|---|-------|-------|--|-------|-------|--|-------|-------|--|-------|-------|---|-------|-------|
| | Mol % | Vol % | Wt % | Mol % | Vol % | Wt % | Mol % | Vol % | Wt % | Mol % | Vol % | Wt % | Mol % | Vol % | Wt % |
| (Mg _{1-x} Fe _x)SiO ₃ | 94.18 | 93.54 | 93.55 | 75.61 | 84.16 | 84.44 | 65.51 | 77.84 | 78.37 | 60.4 | 73.8 | 74.33 | 55.99 | 72.87 | 73.74 |
| (Mg _{1-y} Fe _y)O | 0 | 0 | 0 | 19.69 | 9.97 | 9.64 | 30.03 | 16.23 | 15.59 | 34.41 | 19.11 | 18.45 | 42.74 | 25.28 | 24.37 |
| CaSiO ₃ | 5.82 | 6.46 | 6.45 | 4.7 | 5.85 | 5.92 | 4.46 | 5.93 | 6.04 | 5.19 | 7.09 | 7.22 | 1.27 | 1.85 | 1.89 |

Table 3. Adiabats for lower mantle minerals. $x = 0.125$, $y = 1875$.

| Pressure (GPa) | $\text{Mg}_{1-y}\text{Fe}_y\text{O}$ HS Temperature (K) | $\text{Mg}_{1-y}\text{Fe}_y\text{O}$ MS Temperature (K) | $\text{Mg}_{1-x}\text{Fe}_x\text{SiO}_3$ Temperature (K) | CaSiO_3 Temperature (K) |
|----------------|--|--|---|-------------------------------------|
| 23 | 1873.00 | 1873.00 | 1873.00 | 1873.00 |
| 30 | 1945.85 | 1945.85 | 1927.92 | 1929.92 |
| 40 | 2050.38 | 2050.38 | 2006.76 | 2011.78 |
| 50 | 2144.59 | 2144.59 | 2078.87 | 2086.67 |
| 60 | 2230.87 | 2238.41 | 2145.39 | 2155.80 |
| 70 | 2310.84 | 2328.82 | 2207.19 | 2220.08 |
| 80 | 2385.71 | 2438.50 | 2264.98 | 2280.21 |
| 90 | 2456.34 | 2556.66 | 2319.33 | 2336.73 |
| 100 | 2523.40 | 2672.30 | 2370.71 | 2390.09 |
| 110 | 2587.40 | 2782.20 | 2419.51 | 2440.64 |
| 120 | 2648.73 | 2884.95 | 2466.06 | 2488.70 |
| 125 | 2678.49 | 2932.98 | 2488.58 | 2511.87 |

Table 4. Adiabats for lower mantle aggregates with fp in MS state.

| Pressure (GPa) | Perovskite Only Temperature (K) | Chondritic Temperature (K) | Pyrolite Temperature (K) | Peridotite Temperature (K) | Harzburgite Temperature (K) |
|----------------|------------------------------------|-------------------------------|-----------------------------|-------------------------------|--------------------------------|
| 23 | 1873.00 | 1873.00 | 1873.00 | 1873.00 | 1873.00 |
| 30 | 1928.04 | 1929.67 | 1930.64 | 1931.13 | 1931.97 |
| 40 | 2007.05 | 2010.99 | 2013.33 | 2014.52 | 2016.54 |
| 50 | 2079.32 | 2085.24 | 2088.76 | 2090.56 | 2093.59 |
| 60 | 2149.18 | 2153.92 | 2158.59 | 2161.02 | 2165.02 |
| 70 | 2207.92 | 2218.68 | 2224.83 | 2228.17 | 2233.42 |
| 80 | 2265.85 | 2281.19 | 2289.55 | 2294.41 | 2301.50 |
| 90 | 2320.32 | 2341.75 | 2352.92 | 2359.78 | 2369.19 |
| 100 | 2371.81 | 2399.31 | 2413.30 | 2422.18 | 2433.94 |
| 110 | 2420.71 | 2453.19 | 2469.59 | 2480.21 | 2494.04 |
| 120 | 2467.35 | 2503.53 | 2521.81 | 2533.77 | 2549.28 |
| 125 | 2489.90 | 2527.55 | 2546.59 | 2559.08 | 2575.28 |